





Microfluidic analog of an opposed-jets device

Cite as: Appl. Phys. Lett. **114**, 223701 (2019); <https://doi.org/10.1063/1.5097850>

Submitted: 28 March 2019 . Accepted: 17 May 2019 . Published Online: 05 June 2019

S. J. Haward , C. C. Hopkins , K. Toda-Peters , and A. Q. Shen 



View Online



Export Citation



CrossMark

ARTICLES YOU MAY BE INTERESTED IN

[Photoconductive terahertz detectors with 105 dB peak dynamic range made of rhodium doped InGaAs](#)

Applied Physics Letters **114**, 221103 (2019); <https://doi.org/10.1063/1.5095714>

[Ultrafast photocarrier dynamics in a 3D Dirac semimetal Cd₃As₂ film studied with terahertz spectroscopy](#)

Applied Physics Letters **114**, 221102 (2019); <https://doi.org/10.1063/1.5086085>

[High temperature characteristics of a 2 μm InGaSb/AlGaAsSb passively mode-locked quantum well laser](#)

Applied Physics Letters **114**, 221104 (2019); <https://doi.org/10.1063/1.5096447>



**THE WORLD'S RESOURCE FOR
VARIABLE TEMPERATURE
SOLID STATE CHARACTERIZATION**



WWW.MMR-TECH.COM

OPTICAL STUDIES SYSTEMS

SEEBECK STUDIES SYSTEMS

MICROPROBE STATIONS

HALL EFFECT STUDY SYSTEMS AND MAGNETS

Microfluidic analog of an opposed-jets device

Cite as: Appl. Phys. Lett. **114**, 223701 (2019); doi: [10.1063/1.5097850](https://doi.org/10.1063/1.5097850)

Submitted: 28 March 2019 · Accepted: 17 May 2019 ·

Published Online: 5 June 2019



View Online



Export Citation



CrossMark

S. J. Haward,^{a)}  C. C. Hopkins,  K. Toda-Peters,  and A. Q. Shen 

AFFILIATIONS

Okinawa Institute of Science and Technology, Onna-son, Okinawa 904-0495, Japan

^{a)}Electronic mail: simon.haward@oist.jp

ABSTRACT

A fully three-dimensional (3D) stagnation point microfluidic device is fabricated that, similar to the classical opposed-jet apparatus, can be operated in either a uniaxial or a biaxial extensional flow mode with an easily controllable strain rate. The microchannel is etched inside fused silica and has optical access through all three planes. A detailed characterization of the Newtonian flow field by microparticle image velocimetry confirms the expected nature of the flow and compares well with the prediction of 3D numerical simulations. Flow-induced birefringence of a model polymer solution demonstrates the extension of macromolecules in both modes of operation and the potential use of the device for quantitative rheo-optical studies. This microfluidic opposed jet device could also be used for examining the deformation and dynamics of drops, cells, fibers, and single molecules in well-defined and relevant flow fields.

© 2019 Author(s). All article content, except where otherwise noted, is licensed under a Creative Commons Attribution (CC BY) license (<http://creativecommons.org/licenses/by/4.0/>). <https://doi.org/10.1063/1.5097850>

Extensional flows with a stagnation point are extremely effective at stretching fluid elements and have wide utility for the study of the deformation and breakup of bubbles, drops, fibers, and cells,^{1–4} for observing macromolecular dynamics^{5–7} and elastic instabilities,^{8,9} and for performing extensional rheometry of complex fluids.^{10,11}

Classically, three instruments have been used to generate stagnation point flows in the laboratory. The first is the four-roll mill presented by Taylor,¹² which can be used to generate a planar elongational flow and was employed to examine the deformation and breakup of droplets trapped at the stagnation point. The second is the opposed-jet apparatus of Frank *et al.*,¹³ in which two nozzles face each other immersed in a bath of fluid. Two modes of operation are possible. If the fluid is sucked into the nozzles (“sucking mode”), a uniaxial extensional flow is generated along the axis of the nozzles. If the fluid is ejected from the nozzles (“blowing mode”), an equibiaxial extensional flow is generated in the center-plane perpendicular to the nozzle axis. The opposed jets were used in pioneering studies of macromolecular dynamics (summarized in Ref. 14), and were even developed into a commercial extensional rheometer (the Rheometrics RFX).¹⁵ However, interest in the device declined as it was realized that measurements were inherently affected by inertia and because no satisfactory method could be devised to separate shear and elongational stresses.¹⁶ The third classical stagnation point flow device is the cross-slot geometry, first presented by Scriven *et al.*,¹⁷ which is formed from two bisecting rectangular channels. If fluid is injected into two opposing inlets and withdrawn from two opposing outlets, a planar

stagnation point elongational flow is generated. The device has had success as a planar extensional rheometer since shear stresses can be directly measured from the pressure drop around one corner of the geometry, allowing elongational stresses to be isolated from the total.¹⁸ The device is also readily reduced to the microscale, minimizing required fluid volumes and obviating complications arising from inertia. The cross-slots continue to be widely used among the microfluidics community for both fundamental and applied studies (see the review in Ref. 19).

Microfluidic analogs have since been developed for the four-roll mill.^{20–22} These devices have multiple inlets and outlets and enable the generation of various flow types²³ ranging between solid body rotation and planar elongation by varying the inlet:outlet flow rate ratio (analogous to regulating the rotation rates of the individual rollers in the classical set up).

In this work, we present the first experimental realization of a microfluidic opposed jet analog; the operating principle of which is illustrated in Fig. 1. The system consists of three mutually bisecting channels of square cross section. If the fluid is injected at a rate Q_{in} through two pairs of opposed inlets, and is withdrawn at a rate $Q_{out} = 2Q_{in}$ from the remaining pair of opposed inlets, a uniaxial extensional flow is generated along the outlet axis [see Fig. 1(a)]. This is analogous to the opposed jets operating in sucking mode. If the flow is simply reversed, as illustrated in Fig. 1(b), equibiaxial extensional flow is generated over the outlet plane. This is analogous to the opposed jets operating in blowing mode.

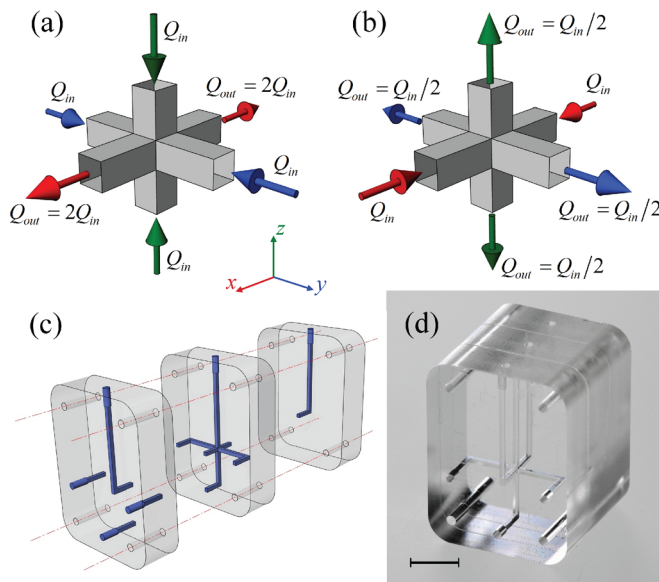


FIG. 1. Principle and realization of the microfluidic opposed-jet analog. (a) Pumping fluid in through two-pairs of opposed inlets (here along the y and z directions) and withdrawing fluid from the third pair of opposed outlets, generates a uniaxial extensional flow along the x -axis. (b) By performing the reverse operation, a biaxial extensional flow is generated over the $x = 0$ plane. (c) Schematic diagram of the device designed to be assembled from three pieces of 5 mm thick fused silica. The microchannel is colored in blue for clarity. (d) A photograph of the final assembled device. The scale bar represents 5 mm in the foreground.

The system presented in Fig. 1 has a number of important advantages over the classical opposed jets. Most obviously, by enclosing the entire fluidic system in microscale channels the required volume of the test fluid is reduced, as are inertial contributions to the fluid dynamics. Also, in contrast to the classical system, in the microfluidic analog, pressure measurements made across an inlet and an outlet could be used to quantify shearing contributions to the total pressure loss (by a similar method to that employed in the planar cross-slot geometry¹⁸), enabling uni- and biaxial extensional viscosity measurements. We point out that while the planar cross-slot type geometries have been quite successful as extensional rheometers,^{10,18} in most practical cases (such as thread, fiber, and film formation, and inkjet printing) elongational flows are either uniaxial or biaxial, and different extensional viscosity functions are expected in each case.²⁴ Thus, the development of uni- and biaxial extensional rheometers is of significant practical importance. Note also that in the microfluidic opposed-jet analog, by imposing different flow rates in the two pairs of outlet channels a general, or “ellipsoidal,” biaxial extension could be generated,²⁴ which is not possible in the classical system.

Although in principle the set up illustrated in Figs. 1(a) and 1(b) appears quite straightforward and it has been presented before in a numerical study of elastic instabilities in uniaxial and biaxial stagnation point flows,²⁵ constructing such a device for experimental measurements is not trivial. The challenge is particularly great given that optical access to the central cross-over region is required not only for confirmation of the flow field, but also for rheo-optical (birefringence) measurements with complex fluids, or for the observation of single molecule dynamics, for instance.

By using the high resolution ($\approx 1\ \mu\text{m}$) subtractive three-dimensional (3D) printing technique of selective laser-induced etching (SLE),²⁶ we have achieved the fabrication of a microfluidic opposed-jet analog device in fused silica glass, which allows good optical access through four of the six sides (and even full optical transmission through two of the three planes), see Figs. 1(c) and 1(d). The device is fabricated using three pieces of 5 mm thick fused silica (the thickest that can be used in the SLE instrument in our lab). As shown in Fig. 1(c), the active region of the device where the three channels bisect (with sharp unrounded corners) and the extensional flows are generated is fabricated in a single central piece of glass. Four of the channels leading to/from the central cross-over region have uninterrupted straight sections of length $>10 \times L$, where L is the side-length of the square cross-section channels. This ensures that the flow can become fully developed prior to the intersection when the device is operated in either uni- or biaxial flow mode. The remaining two channels are necessarily shorter as their length is restricted by the 5 mm thickness of the glass; these two channels are always used as outlets so that their short length has a minimal impact on the flow and its stability at the upstream intersection. The central piece of glass is sandwiched between two additional 5 mm thick glass layers that contain extensions of the short outlet channels and also allow some of the channels to be redirected through 90° , thus keeping four of the six sides free of inlet and outlet connections. The three pieces are accurately assembled using locating pins passed through holes etched in the four corners of each part and are bonded together using ultraviolet-curing epoxy resin. A fully assembled device, with channels of side length $L = 550\ \mu\text{m}$, is shown in the photograph in Fig. 1(d). Stainless steel tubing connectors are bonded to the inlet and outlet holes using two-part epoxy resin and are joined by silicone tubing to Hamilton Gastight syringes. The flow is driven using six individually controllable neMESYS syringe pumps (Cetoni, GmbH).

Our first experiments involve the use of microparticle image velocimetry (μ -PIV)^{27,28} in order to confirm the expected flow field in the device under the two basic modes of operation. For these experiments, we use a Newtonian fluid (50 wt. % aqueous glycerol, viscosity $\eta = 5\ \text{mPa}\cdot\text{s}$, and density $\rho = 1123.6\ \text{kg}\cdot\text{m}^{-3}$ at 25°C) seeded with $5\ \mu\text{m}$ diameter fluorescent microspheres (PS-Fluored, MicroParticles GmbH). A $5\times$ objective lens focuses on the plane of interest within the microdevice, which is placed in its desired orientation on the imaging stage of an inverted microscope (Nikon Eclipse Ti). The microscope is equipped with a volume illumination μ -PIV system (TSI Inc.) consisting of a dual-pulsed laser (Continuum Terra-PIV) and a high speed camera (Phantom Miro). Pairs of laser pulses with user-specified time separation δt excite fluorescence of the microparticles and their positions are captured in a corresponding pair of images. Particle positions are cross-correlated in interrogation areas to obtain the local particle displacement over the time δt and hence local velocity vector, denoted as $\mathbf{v} = (u, v, w)$. Note that only in-plane velocity components are acquired. The measurement depth over which out of plane particles contribute to the determination of velocity vectors is $\delta m \approx 170\ \mu\text{m}$ or $\approx 0.3L$.²⁸

Figure 2 summarizes the results of μ -PIV experiments conducted under uniaxial extension. Figure 2(a) shows the velocity magnitude $|\mathbf{v}|$, normalized by the average outflow velocity $U_{\text{out}} = Q_{\text{out}}/L^2$, for uniaxial elongation as viewed in the $z = 0$ plane, showing inflow along y and the outflow accelerating along x from a central stagnation point

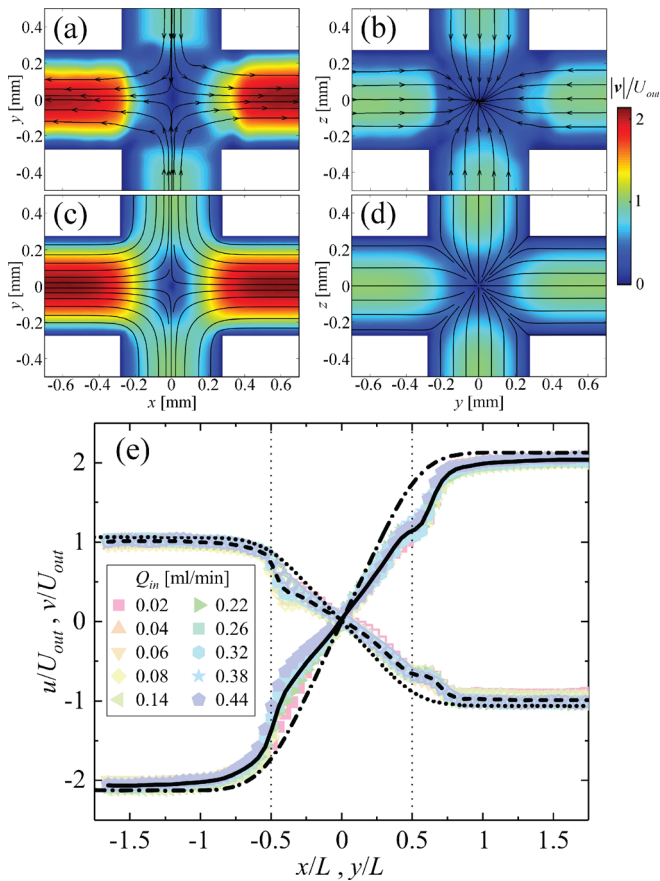


FIG. 2. Newtonian fluid flow in uniaxial extension. (a) and (b) Experimentally measured and (c) and (d) numerically predicted normalized velocity magnitude fields with superimposed streamlines as viewed in the $z=0$ and $x=0$ planes, respectively. (e) Normalized experimental velocity profiles along the x and y axes for a range of imposed inlet flow rates. The solid and dashed lines are the averages of all the experimental data along the x -axis (outlet) and y -axis (inlet), respectively. The dashed-dotted and dotted lines are the numerical predictions of the profiles along the x -axis and y -axis, respectively.

into the outlet channels. Figure 2(b) shows a similar contour plot measured in the $x=0$ plane, showing how the inflow along the y and z directions converges into a “sinklike” central stagnation point located on the x -axis. The ability to view the flow from various planes is a feature of this device that may provide some interesting new opportunities for deformation dynamics studies and is not possible with conventional opposed jets since the nozzles themselves obscure the view along the axial direction. The experimental velocity fields in Figs. 2(a) and 2(b) are in good qualitative agreement with the results of finite-element numerical simulations (performed using COMSOL Multiphysics), as shown in Figs. 2(c) and 2(d). The numerical method solves the equations of motion and mass conservation for laminar flow of a Newtonian incompressible fluid, assuming no-slip boundary conditions on all walls and applying fixed pressure at inlets and outlets. The mesh is composed of 321 370 tetrahedral elements. The Reynolds number $Re = \rho U_{out} L / \eta = 4.4$ and channels are long enough to ensure fully developed flow upstream of the central cross region.

For a range of inlet flow rates, Fig. 2(e) shows normalized velocity profiles measured along the outlet (x) and one inlet (y) axis. Over this range of Q_{in} , $0.3 \lesssim Re \lesssim 6$, indicating that inertial effects are moderate. Consequently, the experimental data collapse well. The normalized experimental velocity profiles averaged over the various imposed flow rates compare well with the numerical predictions. The extensional rate along the outlet axis, averaged between the outlet channel mouths (i.e., $-0.5L \leq x \leq 0.5L$), is $\dot{\epsilon}_{xx} = \partial u / \partial x = 2.6 U_{out} / L$ (experimental) and $\dot{\epsilon}_{xx} = 3.5 U_{out} / L$ (numerical). We attribute the discrepancy of $\approx 25\%$ to the significant (relative to within the inlet and outlet channels) out of plane motion of particles in the central cross over region. This is likely to cause an error in the determination of planar velocity vectors due to the appreciable measurement depth of the μ -PIV set up, $\delta m \approx 0.3L$. The extensional rate along the inlet axis is $\dot{\epsilon}_{yy} = \partial v / \partial y \approx -0.5 \dot{\epsilon}_{xx}$ in both the experimental and the numerical results, as expected for a uniaxial extensional flow.

The results of μ -PIV experiments conducted under equibiaxial extension are summarized in Fig. 3. Here, we only report data from one plane ($x=0$) showing how the flow in the four outlet channels appears to emerge from a “sourcelike” central stagnation point located on the x -axis, Figs. 3(a) and 3(b). The normalized experimental velocity magnitude field [Fig. 3(a)] is again in reasonable qualitative agreement with a numerical simulation [Fig. 3(b)]. Normalized velocity profiles measured along the two outlet axes for a range of experimental

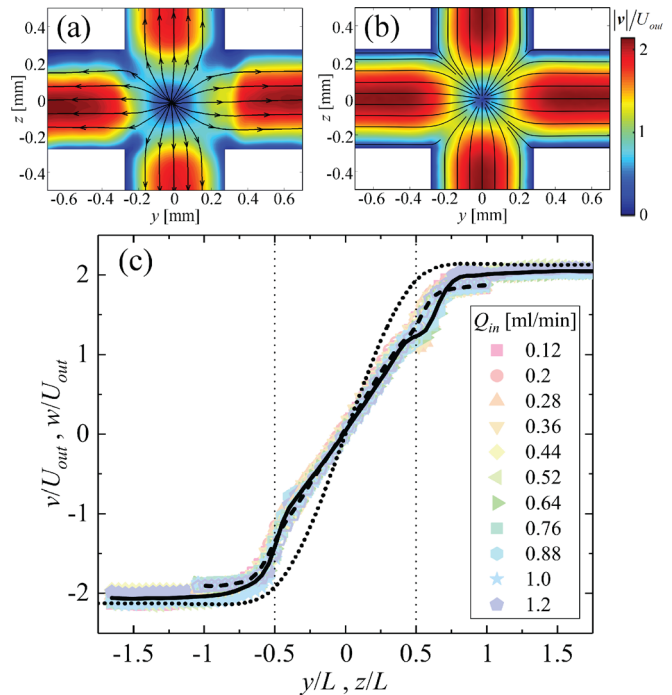


FIG. 3. Newtonian fluid flow in biaxial extension. (a) Experimentally measured and (b) numerically predicted normalized velocity magnitude fields in the $x=0$ plane. (c) Normalized experimental velocity profiles along the y and z axes for a range of imposed inlet flow rates. The solid and dashed lines are the averages of all the experimental data along the y -axis and z -axis (i.e., the two outlets), respectively. The dotted line is the numerically predicted velocity profile along an outlet (i.e., y or z) axis.

Q_{in} values show good collapse in Fig. 3(c). The average experimental elongation rates between the outlet channel mouths are $\dot{\epsilon}_{yy} \approx \dot{\epsilon}_{zz} \approx 2.8U_{out}/L$. The numerically predicted extensional rates along the outlet axes are $\dot{\epsilon}_{yy} = \dot{\epsilon}_{zz} \approx 3.8U_{out}/L$. As in uniaxial extension, the discrepancy is of $\approx 25\%$, which is attributed to the measurement depth of the μ -PIV set up. It will be instructive in future to confirm this assertion by using a state-of-the-art stereoscopic particle tracking velocimetry instrument able to perform volumetric three-component velocimetry with high spatial resolution.²⁹

As a demonstration of both the good optical quality of our microfluidic device and of the possibility of using it to study macromolecular dynamics under uniaxial and biaxial extension, we have also performed quantitative birefringence imaging on a model dilute polymer solution. The fluid is a 1400 ppm (weight) solution of 7 MDa atactic polystyrene (aPS) in the thermodynamically good organic solvent trimesyl phosphate (TCP). The overlap concentration is $c^* \approx 2000$ ppm.³⁰ The fluid is weakly shear-thinning with a zero-shear viscosity $\eta_0 \approx 130$ mPa s and has a relaxation time $\lambda \approx 40$ ms.³⁰ For the measurement, we employ an Exicor MicroImager (Hinds Instruments Inc.), which is composed of a 532 nm light source, photoelastic modulators on either side of the sample, a $10\times$ magnification Mitutoyo objective lens focused on the measurement plane, and a 2048×2048 pixel camera.^{31–33} The system provides spatially resolved ($\approx 0.55 \mu\text{m}/\text{pixel}$) values for the retardation R and the orientation of the fast optical axis. The birefringence is directly related to the retardation by $\Delta n = R/\ell$, where ℓ is the optical path length through the birefringent material. As shown in Fig. 4(a), at low flow rates no birefringence can be measured and the orientation angle map is composed of uniform random noise. At progressively higher flow rates [Figs. 4(b) and 4(c)], a birefringent signal is registered in a rather broad region around the outlet (x) axis. The orientation angle map indicates that the fast axis is aligned along the outflow direction, as expected since for aPS the fast optical axis is aligned with the polymer backbone. The plot in Fig. 4(d) shows profiles of the retardation R taken along the y -axis through the regions of high birefringence. Clearly there is a progressive increase in the signal as $\dot{\epsilon}_{xx}$ is incremented, indicating that the polymer molecules become progressively more oriented. Interestingly, there is a consistent dip in the signal close to $y = 0$, i.e., along the outlet axis. This has also been observed in the classical opposed-jet experiments and referred to as a birefringent “pipe”.³⁴ The phenomenon is explained by strong flow modification due to the extensional viscosity of the polymer.³⁵

In equibiaxial extension, we could also measure a birefringent signal in the $z = 0$ plane, as shown in Figs. 5(a)–5(c) for progressively increasing values of Q_{in} . In this case, the polymer is oriented in a very thin birefringent sheet over the $x = 0$ plane. Note that we could not measure any retardation when we viewed the flow in the $x = 0$ plane, which is most likely explained by the extremely short optical path length through the oriented material along the x direction. By considering the ratio of the optical path length along x (ℓ_x , clearly $\approx 10 \mu\text{m}$ from Fig. 5) compared with that along either y or z ($\ell_y = \ell_z \sim L = 550 \mu\text{m}$), it is evident that the expected retardation when viewing along x will be more than an order of magnitude smaller than when viewing along y or z . Since the detection limit of the birefringence imaging system employed is ≈ 0.5 nm, and the range of retardation shown in Fig. 5 is $0 < R < 4$ nm, this explains the absence of a clear retardation signal when viewing in the yz plane. Profiles of the

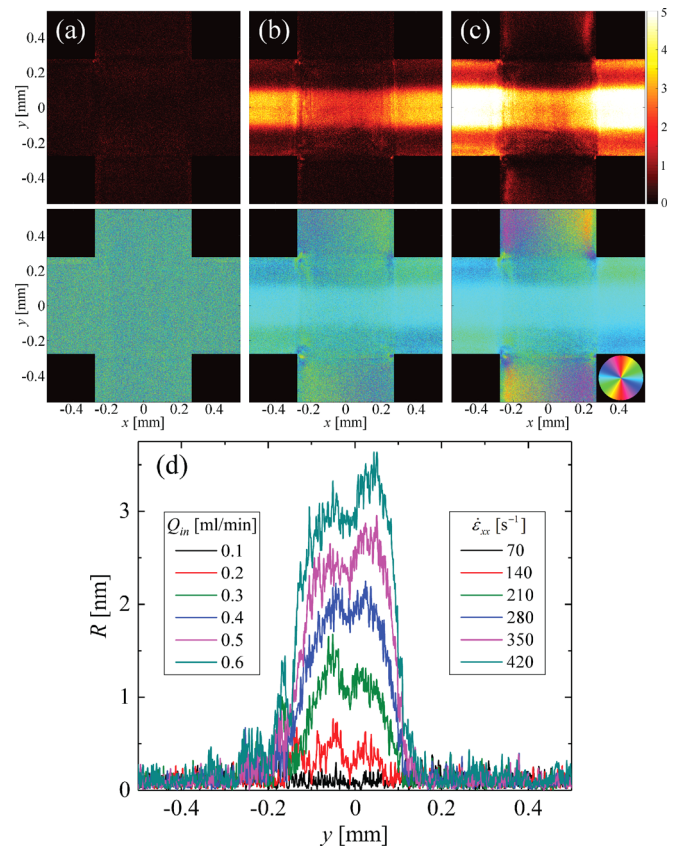


FIG. 4. Birefringence visualized in the $z = 0$ plane for uniaxial extensional flow of an aPS in TCP solution. Top row shows the retardation R with color scale in nanometers, bottom row shows the corresponding orientation of the fast optical axis for: (a) $Q_{in} = 0.1$ ml/min, $\dot{\epsilon}_{xx} \approx 70$ s $^{-1}$, (b) $Q_{in} = 0.4$ ml/min, $\dot{\epsilon}_{xx} \approx 280$ s $^{-1}$, (c) $Q_{in} = 0.6$ ml/min, and $\dot{\epsilon}_{xx} \approx 420$ s $^{-1}$. (d) Profiles of the retardation measured along the y -axis for a range of imposed inlet flow rates.

retardation taken across the birefringent sheet along the x -axis [Fig. 5(d)] show a progressive increase in the birefringence as the flow rate is incremented. Interestingly though, for similar elongation rates along the outlets, the retardation is generally much lower in biaxial than in uniaxial extension. This may be explained by the likelihood of a radial distribution of molecular orientations over the $x = 0$ plane, with molecules on the z -axis most likely to be oriented in the z direction (i.e., along the direction of light propagation) which would therefore not be expected to contribute to the measured signal. Between $\dot{\epsilon}_{yy} = 266$ and $\dot{\epsilon}_{yy} = 305$ s $^{-1}$ there is a dramatic increase in the retardation to a value comparable with that seen in uniaxial extension. However, we note that the sheet of birefringence is no longer localized on the $x = 0$ plane, which is a likely indication that the flow field has lost stability. Although this instability remains to be properly investigated, we are confident in the accuracy of our flow control and we note that the Reynolds number of the flow is quite moderate at its onset ($Re \approx 4$), so we assume it to be an elasticity-induced flow asymmetry.^{8,9,25}

In summary, we have presented the first microfluidic analog of an opposed-jet apparatus that can generate both uniaxial and biaxial stagnation point extensional flow fields with easily controlled extensional

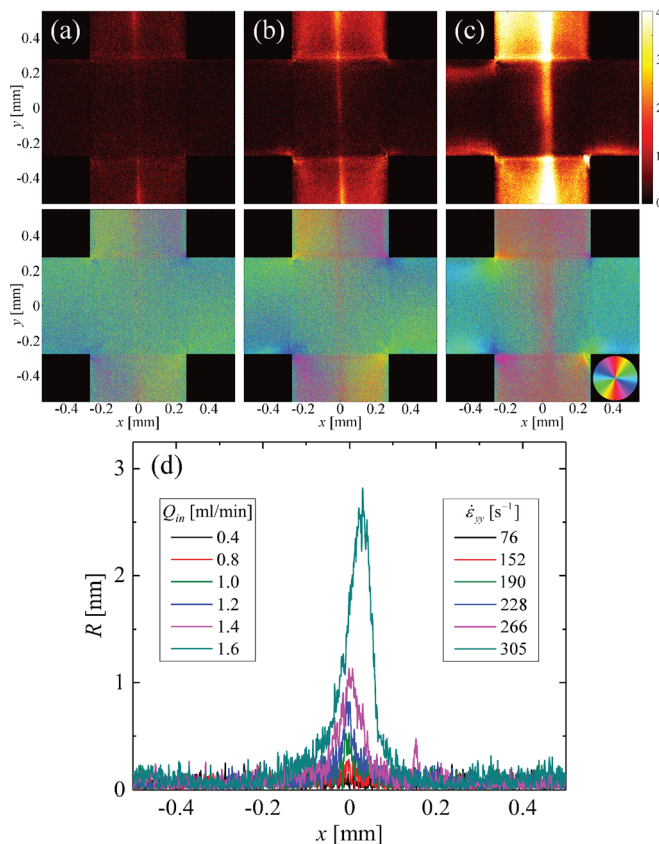


FIG. 5. Birefringence visualized in the $z=0$ plane for biaxial extensional flow of an aPS in TCP solution. The top row shows the retardation R with a color scale in nanometers; the bottom row shows the corresponding orientation of the fast optical axis for: (a) $Q_{in} = 0.8$ ml/min, $\dot{\epsilon}_{yy} \approx 152$ s⁻¹, (b) $Q_{in} = 1.2$ ml/min, $\dot{\epsilon}_{yy} \approx 228$ s⁻¹, (c) $Q_{in} = 1.6$ ml/min, and $\dot{\epsilon}_{yy} \approx 305$ s⁻¹. (d) Profiles of the retardation measured along the x -axis for a range of imposed inlet flow rates.

rates. The device has interesting features that are not offered by the classical opposed jets, such as the ability to observe the region of extensional flow from multiple perspectives and also of generating a general biaxial, as opposed to simply equibiaxial, flow. In addition, the small size scale reduces inertial effects in the flow and also reduces the volume of fluid required for an experiment. Flow-induced birefringence measurements on a dilute polymer solution demonstrate that macromolecular orientation can occur under both modes of flow and also the high optical quality of the fused silica-fabricated device. We believe that the device should be amenable to numerical optimization in order to homogenize the flow fields, as has been done already for various planar extensional flow geometries.^{11,36,37} This could provide for an interesting and novel microfluidic uniaxial and biaxial extensional rheometer based on either rheo-optical measurements or by using pressure drop measurements to isolate extensional stresses from the total, similar to the planar cross-slot device. Furthermore, the device could be used for understanding deformation and dynamics of bubble drops, fibers, cells, and single molecules in well-defined flow fields relevant to widespread applications (e.g., fiber spinning, particle sedimentation, inkjet printing, spin coating, blow molding, etc.).

We gratefully acknowledge the support from the Okinawa Institute of Science and Technology Graduate University, with subsidy funding from The Cabinet Office, Government of Japan. S.J.H. and A.Q.S. also acknowledge Grant Nos. 17K06173, 17J00412, 18K03958, and 18H01135 from the Japan Society for the Promotion of Science.

REFERENCES

- V. Kantsler, E. Segre, and V. Steinberg, *Phys. Rev. Lett.* **101**, 048101 (2008).
- D. R. Gossett, H. T. K. Tse, S. A. Lee, Y. Ying, A. G. Lindgren, O. O. Yang, J. Rao, A. T. Clark, and D. Di Carlo, *Proc. Natl. Acad. Sci. U. S. A.* **109**, 7630 (2012).
- V. Kantsler and R. E. Goldstein, *Phys. Rev. Lett.* **108**, 038103 (2012).
- C. de Loubens, J. Deschamps, G. Boedec, and M. Leonetti, *J. Fluid Mech.* **767**, R3 (2015).
- T. T. Perkins, D. E. Smith, and S. Chu, *Science* **276**, 2016 (1997).
- D. E. Smith, H. P. Babcock, and S. Chu, *Science* **283**, 1724 (1999).
- C. M. Schroeder, H. P. Babcock, E. S. G. Shaqfeh, and S. Chu, *Science* **301**, 1515 (2003).
- P. E. Arratia, C. C. Thomas, J. Diorio, and J. P. Gollub, *Phys. Rev. Lett.* **96**, 144502 (2006).
- R. J. Poole, M. A. Alves, and P. J. Oliveira, *Phys. Rev. Lett.* **99**, 164503 (2007).
- S. J. Haward, T. J. Ober, M. S. N. Oliveira, M. A. Alves, and G. H. McKinley, *Soft Matter* **8**, 536 (2012).
- S. J. Haward, M. S. N. Oliveira, M. A. Alves, and G. H. McKinley, *Phys. Rev. Lett.* **109**, 128301 (2012).
- G. I. Taylor, *Proc. R. Soc. London, Ser. A* **146**, 501 (1934).
- F. C. Frank, A. Keller, and M. R. Mackley, *Polymer* **12**, 467 (1971).
- A. Keller and J. A. Odell, *Colloid Polym. Sci.* **263**, 181 (1985).
- G. G. Fuller, C. A. Cathey, B. Hubbard, and B. E. Zebrowski, *J. Rheol.* **31**, 235 (1987).
- P. Dontula, M. Pasquali, L. E. Scriven, and C. W. Macosko, *Rheol. Acta* **36**, 429 (1997).
- O. Scriven, C. Berner, R. Cressely, R. Hocquart, R. Sellin, and N. S. Vlachos, *J. Non-Newtonian Fluid Mech.* **5**, 475 (1979).
- S. J. Haward, V. Sharma, and J. A. Odell, *Soft Matter* **7**, 9908 (2011).
- S. J. Haward, *Biomicrofluidics* **10**, 043401 (2016).
- S. D. Hudson, F. R. Phelan, M. D. Handler, J. T. Cabral, K. B. Migler, and E. J. Amis, *Appl. Phys. Lett.* **85**, 335 (2004).
- J. S. Lee, R. Dylla-Spears, N. P. Teclerian, and S. J. Muller, *Appl. Phys. Lett.* **90**, 074103 (2007).
- J. Deschamps, V. Kantsler, E. Segre, and V. Steinberg, *Proc. Natl. Acad. Sci. U. S. A.* **106**, 11444 (2009).
- G. Astarita, *J. Non-Newtonian Fluid Mech.* **6**, 69 (1979).
- C. J. S. Petrie, *J. Non-Newtonian Fluid Mech.* **137**, 15 (2006).
- A. M. Afonso, M. A. Alves, and F. T. Pinho, *J. Non-Newtonian Fluid Mech.* **165**, 743 (2010).
- N. Burshstein, S. T. Chan, K. Toda-Peters, A. Q. Shen, and S. J. Haward, *Curr. Opin. Colloid Interface Sci.* **43**, 1 (2019).
- C. D. Meinhart, S. T. Wereley, and M. H. B. Gray, *Meas. Sci. Technol.* **11**, 809 (2000).
- S. T. Wereley and C. D. Meinhart, *Annu. Rev. Fluid Mech.* **42**, 557 (2010).
- A. Schröder, D. Shanz, D. Michaelis, C. Cierpka, S. Scharnowski, and C. J. Kähler, *Flow, Turbul. Combust.* **95**, 193 (2015).
- F. Del Giudice, S. J. Haward, and A. Q. Shen, *J. Rheol.* **61**, 327 (2017).
- C.-Y. Han and Y.-F. Chao, *Rev. Sci. Instrum.* **77**, 023107 (2006).
- S. Nichols, J. Freudenthal, O. Arteaga, and B. Kahr, in *Polarization: Measurement, Analysis, and Remote Sensing XI*, edited by D. B. Chenault and D. H. Goldstein (SPIE-International Society for Optical Engineering, 2014), Vol. 9099, p. 909912.
- S. J. Haward, G. H. McKinley, and A. Q. Shen, *Sci. Rep.* **6**, 33029 (2016).
- A. J. Müller, J. A. Odell, and A. Keller, *J. Non-Newtonian Fluid Mech.* **30**, 99 (1988).
- O. G. Harlen, E. J. Hinch, and J. M. Rallison, *J. Non-Newtonian Fluid Mech.* **44**, 229 (1992).
- K. Zografos, F. Pimenta, M. A. Alves, and M. S. N. Oliveira, *Biomicrofluidics* **10**, 043508 (2016).
- F. Pimenta, R. G. Sousa, and M. A. Alves, *Biomicrofluidics* **12**, 054103 (2018).